DOI: 10.31276/VJSTE.65(4).42-47

Effects of the wheel rotation speed during the melt-spinning process on the structural morphology and the thermoelectric properties of $Ti_{0.5}Zr_{0.5}NiSn$ alloy

Nguyen Van Du[1*], Nguyen Tu[1], Do Quang Trung[1], Noy Sysavanh[2], Manh Trung Tran[3], Tong Thi Hao Tam[4]

[1]Faculty of Fundamental Sciences, Phenikaa University, Yen Nghia Ward, Ha Dong District, Hanoi, Vietnam
[2]Thai Nguyen University of Education, Tan Thinh Ward, Thai Nguyen City, Thai Nguyen Province, Vietnam
[3]Faculty of Materials Science and Engineering, Phenikaa University, Yen Nghia Ward, Ha Dong District, Hanoi, Vietnam
[4]School of Information Technology and Digital Economic, National Economics University, 207 Giai Phong Street, Dong Tam Ward, Hai Ba Trung District, Hanoi, Vietnam

Received 14 February 2023; revised 22 February 2023; accepted 26 May 2023

Abstract:

Half-Heusler alloys based on (Ti, Hf, Zr)NiSn possess excellent mechanical and chemical properties as well as high thermal stability, making them promising materials for high-performance thermoelectric (TE) power generators. However, the high cost of Hf limits its use in these alloys. Therefore, Hf-free (Ti, Zr)NiSn alloys synthesised using a rapid process offer a cost-effective approach to reducing product costs. In this study, we employed the fast synthesis melt-spinning (MS) method to prepare an Hf-free $Ti_{0.5}Zr_{0.5}NiSn$ alloy while systematically optimising MS conditions. We found that by varying the rotation speed of the copper wheel in the MS system from 1000 to 4000 rpm, a marked change in the structural morphology of the melt-spun ribbons occurred. Grain growth during the spark plasma sintering process significantly affected TE properties of the bulk $Ti_{0.5}Zr_{0.5}NiSn$ alloy depending on the structural morphology. As a result, a maximum ZT of ~1.1 at 823 K was achieved for a wheel rotation speed of 3000 rpm, which is comparable to ZT values obtained from the (Ti, Hf, Zr)NiSn-based half-Heusler alloys prepared by other methods.

Keywords: **arc melting, half-Heusler, melt-spinning, spark plasma sintering, TEs.**

Classification numbers: **2.1, 2.3**

1. Introduction

TE materials are essential components in the production of devices used to convert thermal energy into electricity and vice versa. The energy conversion efficiency in TE devices depends largely on the dimensionless figure-of-merit (ZT) of the material. ZT is determined by the relationship between the Seebeck coefficient (S), electrical conductivity (σ), thermal conductivity (K), and absolute temperature T, and is calculated as $ZT=S^2\sigma T/K$ [1, 2]. Various materials have been developed with high TE performance, including Bi_2Te_3-based alloys [3, 4] and skutterudite-based materials [5, 6]. XNiSn (X=Ti, Zr, Hf)-based alloys are interesting research subjects because they possess good mechanical and chemical properties, high thermal stability, and a large power factor (PF-power factor, $PF=S^2\sigma$). These alloys are suitable for applications that harvest waste heat in the medium-to-high temperature range (600 to 900 K) [1, 2, 7, 8]. However, the relatively high thermal conductivity of XNiSn materials compared with other potential materials remains a limitation for improved performance [7, 9, 10].

Efforts to improve the TE efficiency of XNiSn (X=Ti, Zr, Hf) alloys have been undertaken with various approaches. The common approach is to optimise the carrier concentration through donor doping to enhance power factor. At the same time, point defect phonon scattering induced by mass and strain field fluctuations can be achieved by isoelectronic substitutions between Ti, Zr, and Hf at the X site to suppress phonon thermal conductivity [1, 11-15]. To implement these approaches, various synthesis methods such as arc melting combined with the long-term annealing [16-19], the MS method [1, 20], solid phase reactions [21], mechanical alloying [22, 23], self-propagating high temperature [24], levitation melting [7, 25-27], and microwave methods [28] can be used. Among these techniques, MS is known as a fast synthesis process, which has an added advantage of fine-tuning the nanostructure to improve both electrical and thermal properties, thereby enhancing the TE efficiency of the material [1, 20, 29].

Studies on enhancing TE efficiency for a specific material is always of interest. However, for the product to be commercialised, cheap and readily available raw materials are also required. Besides, rapid synthesis methods save time and energy, reducing product costs. In the present work, we selected the Hf-free $Ti_{0.5}Zr_{0.5}NiSn$ alloy along with a fast preparation method like MS for a cost-effective approach. To improve the TE performance of the $Ti_{0.5}Zr_{0.5}NiSn$ alloy, we focused on optimising technology conditions by investigating the effect of the cooling rate induced by varying the copper wheel rotation speed from 1000 to 4000 rpm in the MS system. We found that the structural morphology

*Corresponding author: Email: du.nguyenvan@phenikaa-uni.edu.vn

of $Ti_{0.5}Zr_{0.5}NiSn$ alloy was strongly affected by wheel rotation speed. Nano-grains with uniform shape and size of about 160 nm distributed over the ribbons were observed for wheel rotation speeds of 3000 rpm and higher. The grain growth during the SPS process directly affects the thermal and charge transport properties of the $Ti_{0.5}Zr_{0.5}NiSn$ alloy. As a result, a high ZT value of ~1.1 at ~800 K was achieved for the sample with the optimised wheel rotation speed of 3000 rpm. The results suggest that optimising preparation conditions is vital to improving the ZT of $Ti_{0.5}Zr_{0.5}NiSn$ alloy besides other approaches.

2. Materials and methods

The experimental procedure is shown in Fig. 1. Accordingly, four $Ti_{0.5}Zr_{0.5}NiSn$ alloy ingots, approximately 8 grams each, were prepared using Ti (99.4%, powder), Zr (slug, 99.5%, slug), Ni (99.8%, powder), and Sn (99.99+%, shot) from Alfa Asear by arc melting method under high purity argon gas. The ingots were then placed into graphite crucibles of inner diameter 14 mm with a 4-mm circular nozzle at the bottom for melt spinning. In the MS process, the ingot is heated to a liquid state with a copper induction coil, then injected directly onto the outer surface of the steadily rotating copper wheel (25 cm in diameter) under an Ar gas pressure of 0.2 MPa. The wheel rotation speed was set to 1000, 2000, and 4000 rpm, corresponding to wheel surface speeds of 13.1, 26.2, 39.3, and 52.4 m/s for each melted ingot. The melt-spun ribbons were pulverised into fine powders using an agate mortar and pestle to investigate their TE properties. The ground powders were simultaneously pressed and sintered with a pressure of 65 MPa and temperature of 1,373 K for 1 hour inside the high vacuum chamber of the SPS system. The spark plasma sintered (SPSed) bulk samples were then cut into suitable shapes using precision diamond saws for measurements and analysis.

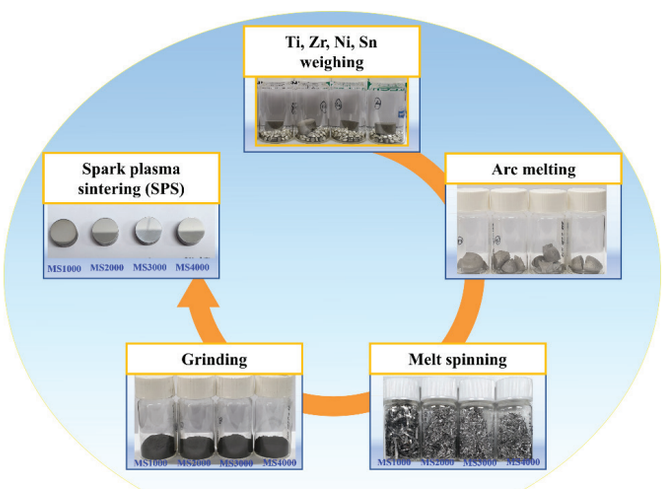

Fig. 1. Experimental procedure for the $Ti_{0.5}Zr_{0.5}NiSn$ alloy.

The morphology, elemental distribution, and chemical composition were investigated using a field emission-scanning electron microscope (FE-SEM) (JSM-7600F, JEOL) with integrated energy-dispersive X-ray spectrometry. The phase purity of the SPSed samples was examined by X-ray diffraction (XRD) using a Rigaku D/max 2500 instrument with Cu Kα (λ=1.5418 Å) radiation operating at 40 kV. The temperature-dependent electrical conductivity and the Seebeck coefficient were simultaneously measured using a ZEM-3 (ULVAC-RIKO) system under low pressure He gas. Thermal conductivity was determined from the thermal diffusivity, measured density, and specific heat. The temperature-dependent thermal diffusivity was measured using NETZSCH LFA 457 equipment. For convenience, the samples examined with wheel rotation speeds of 1000, 2000, 3000, and 4000 rpm were named MS1000, MS2000, MS3000, and MS4000, respectively.

3. Results and discussion

To study the effect of wheel rotation speed on the structural morphology of $Ti_{0.5}Zr_{0.5}NiSn$ alloys, FE-SEM images were taken on the freshly fractured cross-sectional surface of the melt-spun ribbons, as shown in Fig. 2. As the wheel speed increased, the thickness of the ribbons decreased monotonically from 26.3 to 10.2 µm, as shown in Figs. 2A-2D. Due to the difference in cooling rate between the contact and free surfaces of the ribbon, the structural morphology on either side of the ribbons was significantly different. In particular, at a wheel rotation speed of 1000 rpm, grain sizes of 500 nm were observed as well as agglomeration to form larger grains of several µm as shown in Fig. 2A-1, with an enlarged view of the selected area marked by the orange square in Fig. 2A. When the wheel speed increased to 2000 rpm, the obtained ribbons displayed precise layering with two layers formed with different structural morphologies, as shown in Fig. 2B-1. The contact surface of the ribbon exhibited grains with high uniformity in size and shape. Grain sizes less than 200 nm were observed, and the grain boundaries appeared clearer. In contrast, the free side exhibited a similar structure to that obtained in the MS1000 ribbon. For samples with higher wheel speeds of 3000 and 4000 rpm, uniform rapid heat absorption occurred over the entire ribbon thickness resulting in grain formation of a smaller size, roughly 160 nm. Note that nano-scale grain sizes are desired in the nanostructure approach for lowering the thermal conductivity of TE materials, which can only be prepared through long-term ball milling when using other synthesis methods.

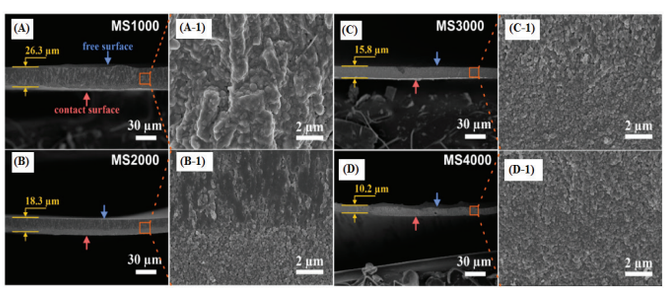

Fig. 2. Cross-section FE-SEM images of the melt-spun ribbons with varying copper wheel speed during MS: (A) MS1000, **(B)** MS2000, **(C)** MS3000, **(D)** MS4000 and **(A-1)-(D-1)** are enlarged views of a selected area marked by orange squares in Figs. 2A-2D, respectively.

To estimate the composition and elemental distribution of the ribbons, EDS analysis was carried out on the cross-section surface of the MS3000 melt-spun ribbons, and the results are shown in Fig. 3. The EDS layered map (Fig. 3A) reveals the elements of the $Ti_{0.5}Zr_{0.5}NiSn$ alloy with a homogenous distribution over the entire observed area. The existence and concentration of Ti (16.36%), Zr (16.83%), Ni (31.88%), and Sn (34.93%), shown in Fig. 3B, suggests that the elemental composition is very close to the stoichiometric composition $Ti_{0.5}Zr_{0.5}NiSn$, indicating that arc melting followed by MS did not change the sample's composition. A uniform distribution of elements over the entire observed area is more clearly confirmed with individual elemental maps, as shown in Figs. 3C-3F.

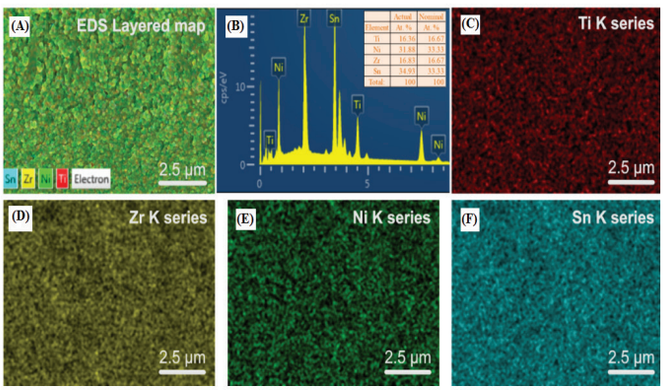

Fig. 3. EDS analysis results for the MS3000 melt-spun ribbon. (A) EDS layered map images; **(B)** EDS spectrum with inset table of elemental concentration (actual composition at at.% compared to nominal composition); **(C-F)** Elemental map images of individual Ti, Zr, Ni, and Sn elements, respectively.

After MS, the ribbons were ground into fine powders and consolidated into bulk via SPS. The evolution of the microstructure during the SPS process was examined by FE-SEM on the fractured cross-sectional surface of the MS1000, MS2000, MS3000, and MS4000 samples. The resulting images are given in Fig. 4. Despite the short sintering time, within 10 minutes, a temperature of 1100°C and applied pressure of 65 MPa showed that large grains formed quickly during the SPS process. Grain sizes greater than 20 μm were observed for the MS1000 sample, while the MS2000 sample demonstrated a grain size distribution in the range of a few μm to 20 μm. MS at 3000 and 4000 rpm produced more uniform grain sizes and shapes with grain sizes of approximately 5 μm as a result of grain growth from smaller nanostructures of melt-spun ribbons, as shown in Figs. 2C-1, 2D-1. In addition, high-density compaction, which favours charge-transport, was performed during the SPS process as shown in the high-resolution FE-SEM images of the MS2000 and MS4000 samples (see Figs. 4 B-1, 4D-1). These results suggested that maintaining nanostructures from melt-spun ribbons for enhanced phonon scattering at grain boundaries requires an ultra-fast sintering process at lower temperatures.

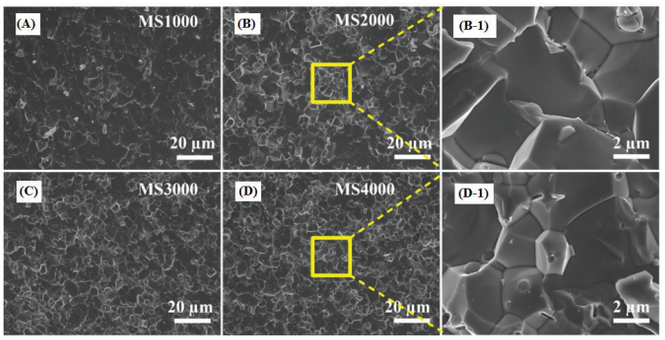

Fig. 4. FE-SEM images taken on the fresh fracture of a cross-section of SPSed bulk (A) MS1000, (B) MS2000, (C) MS3000, and (D) MS4000 samples. (B-1) and **(D-1)** are enlarged views of the selected areas marked by yellow squares in **(B)** and **(D)**, respectively.

In addition to the work conducted, EDS analysis of the bulk SPSed MS3000 was also performed, and the results are presented in Fig. 5. The EDS layered map (Fig. 5A) and elemental maps of Ti, Zr, Ni, and Sn elements (Figs. 5C-5F) confirmed the highly homogeneous distribution of elements over the entire observed area. The chemical composition of the bulk SPSed MS3000 was determined through EDS analysis, and the results are presented in the inset table in Fig. 5B. The analysis identified the amount of Ti 15.82, Ni at 33.13, Zr at 17.11, and Sn at 33.94 at.%. These results indicate that the elemental percentages were consistent with the observed results on the ribbon and did not differ significantly from the stoichiometric composition of $Ti_{0.5}Zr_{0.5}NiSn$.

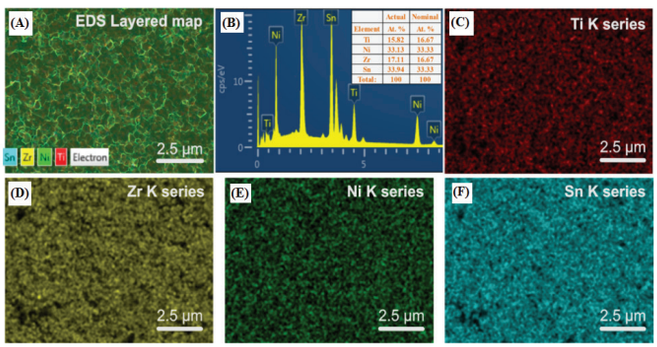

Fig. 5. EDS analysis results for the SPSed MS3000 sample. (A) EDS layered map images; **(B)** EDS spectrum with inset table of elemental concentration (actual composition (at.%) compared to nominal composition); **(C-F)** Elemental map images of individual Ti, Zr, Ni, and Sn elements, respectively.

The XRD analysis results of the SPSed bulk samples melt-spun at different wheel speeds are presented in Fig. 6. All diffraction peaks observed at the crystal planes (111), (200), (220), (311), (222), (400), (311), (420), and (422) in the 2θ angle range from 20 to 80° exhibit a single phase that can be indexed to the cubic half-Heusler crystal structure, consistent with all observed XRD patterns for (Ti, Zr, Hf)NiSn-based alloys in the literature [25, 30-32]. By extending the observation to the main diffraction peaks at the (220) plane, an asymmetrical distribution of those diffraction

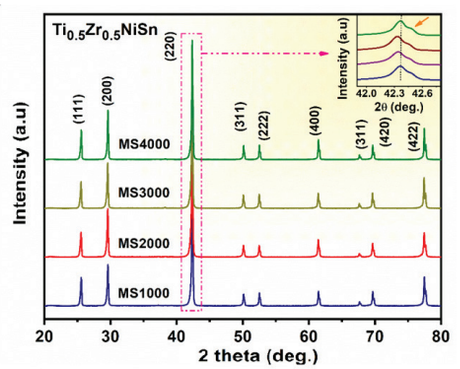

Fig. 6. XRD patterns of bulk $Ti_{0.5}Zr_{0.5}NiSn$ alloys prepared by MS-SPS.

peaks with a high-angle shoulder was observed (Fig. 6). This could be attributed to phase separation into two Ti-rich and Zr-rich phases induced by alloying between Ti and Zr in the crystal. The combined effects of phase separation and alloying between Ti and Zr in the structure could enhance phonon scattering, thus effectively reducing the thermal conductivity of the $Ti_{0.5}Zr_{0.5}NiSn$ alloy.

The temperature-dependent electrical conductivity and Seebeck coefficient are shown in Fig. 7. The electrical conductivity for all samples (Fig. 7A) increases with increasing temperature from room temperature to the maximum measured temperature of 873 K, caused by the thermal excitation of electrons across the energy gap, exhibiting intrinsic semiconductor-like behaviour. With an increase in wheel rotation speed, the electrical conductivity increased from 167 S/cm for MS1000 to the highest value of 194 S/cm for the MS3000 sample. Then, it decreased to 139 S/cm for the MS4000 sample, which was compared at room temperature. The electrical conductivity trend and variation showed an insignificant effect of the rotating wheel speed during the MS process. The rapid grain growth during the SPS process may be responsible for the small changes in microstructure and thus influence the observed variation in the electrical properties of those samples. Besides, decreasing absolute values of the Seebeck coefficients were obtained with increasing temperature for all samples and were negative over the entire measured temperature range, indicating electrons as the major charge carrier. Among the SPSed samples, the highest Seebeck coefficient was achieved for the MS3000 sample at temperatures above 400 K. Large absolute Seebeck coefficients of about 200-280 μV/K achieved for the samples confirmed the high Seebeck coefficient of half-Heusler (Ti, Zr, Hf)NiSn-based alloys as reported from the literature [10, 33]. The high Seebeck coefficient along with a relatively low electrical conductivity could be suitable for doping or substitution donor impurities for optimising carrier concentration to further improve the power factor for this material.

Figure 8A presents the temperature-dependent power factor ($PF=S^2\sigma$) calculated from the measured electrical conductivity and Seebeck coefficient for the $Ti_{0.5}Zr_{0.5}NiSn$ alloys. Due to low electrical conductivity at room temperature, the PF for all SPSed samples exhibited values of around $14x10^{-4}$ W/mK^2. With increased temperature, PF increases rapidly to a peak value at temperatures above 600 K caused by the predominance of the electrical conductivity and then decreases due to the weakening of the Seebeck coefficient at high temperature. The highest PF over the entire temperature range was obtained for the MS3000 sample with a peak of $37.5x10^{-4}$ W/mK^2 at 774 K due to a significant increase in the Seebeck coefficient even though the electrical

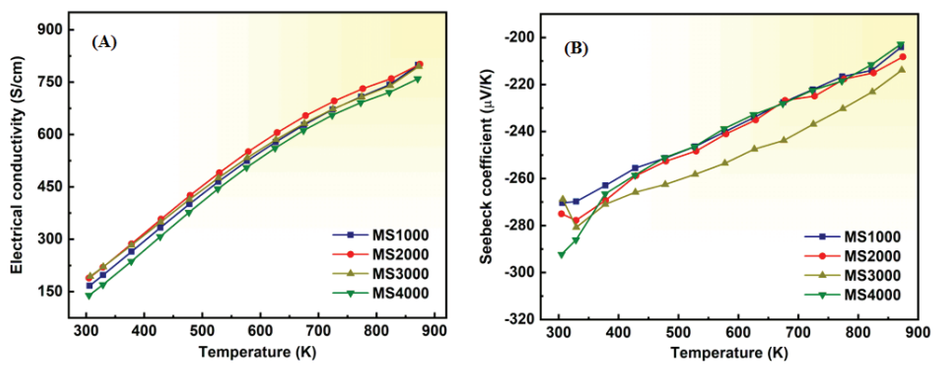

Fig. 7. Temperature dependence of (A) electrical conductivity and (B) Seebeck coefficient of the MS1000, MS2000, MS3000, and MS4000 samples.

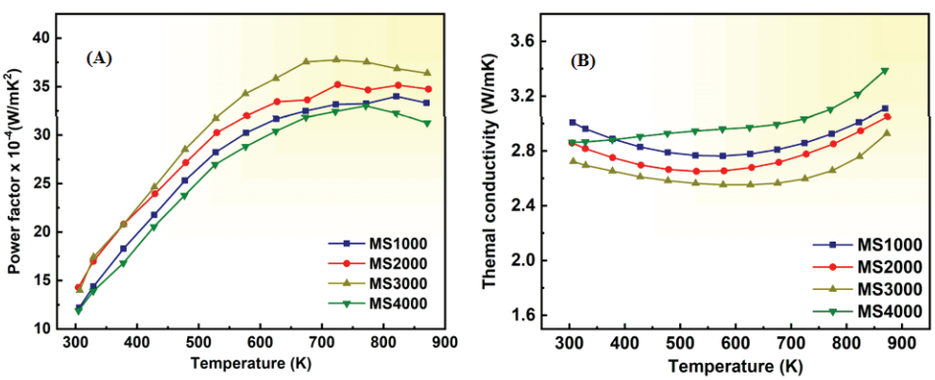

Fig. 8. The temperature dependence of (A) power factor and (B) thermal conductivity of the MS1000, MS2000, MS3000, and MS4000 samples.

conductivity was somewhat worse than that of the MS2000 sample. In addition, obtained relatively high PF obtained in this work suggests that the optimization of preparation conditions can improve the charge transport properties for effective power factor enhancement, besides the approaches to optimising the carrier concentration through doping and/or substitution have been performed for the (Ti, Zr, Hf)NiSn-based alloys [11, 26, 34].

The temperature-dependent thermal conductivity for all samples is presented in Fig. 8B. The thermal conductivity values of the MS1000-MS3000 samples exhibit a similar trend: decreasing at low temperatures, up to 523 K, and increasing with temperatures above 523 K, suggesting bipolar thermal conduction. Thermal conductivity was also found to decrease with wheel rotation speed up to 3000 rpm over all temperatures. This observation could be explained in terms of the combined phonon scattering effects that exist in $Ti_{0.5}Zr_{0.5}NiSn$ alloys. Accordingly, grain growth from a smaller grain structure at the same sintering temperature could lead to an increase in structural disorder, thereby enhancing point defect phonon scattering. Furthermore, the grain boundary density of the MS3000 sample is larger than that of the MS samples with lower wheel rotational speed (see FE-SEM images in Figs. 4A-4C, further contributing to the enhanced phonon scattering at the grain boundaries. As a result, the lowest thermal conductivity of 2.55 W/mK at around 600 K was obtained for the MS3000 sample among investigated samples, which is comparable to the lowest reported values for (Ti, Zr, Hf)NiSn-based half-Heusler alloys [1, 12, 35].

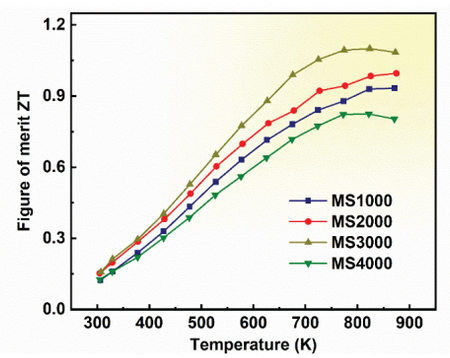

Fig. 9. The temperature dependence of the dimensionless ZT of the MS1000, MS2000, MS3000, and MS4000 samples.

The temperature dependence of the dimensionless ZT is calculated from PF and thermal conductivity and is shown in Fig. 9. With an increase in temperature, the ZT values exhibited a similar trend as the PF obtained for all samples when varying the copper wheel rotation speed from 1000 rpm to 4000 rpm. The combination of high PF and the low thermal conductivity led to a significant enhancement in ZT over the entire measured temperature range for the MS3000 sample of which the highest ZT value of ~1.1 at 823 K was achieved. The obtained ZT of ~1.1 is higher than most reported values for Hf-free (Ti, Zr)NiSn-based half-Heusler alloys prepared by other methods and/or other approaches [12, 18, 19, 36-39].

4. Conclusions

We studied the effects of wheel speed during the melt spinning process on the structural morphology of melt-spun ribbons. Specifically, the morphology, phase formation, and temperature-dependent TE properties of SPSed $Ti_{0.5}Zr_{0.5}NiSn$ bulk samples from melt-spun ribbons. It was found that with an increase in wheel speed, the obtained alloy ribbons had a reduced thickness, more uniform nanograin structure, and the observed grain size of the ribbons decreased to a minimum of 160 nm due to increase in cooling rate induced by high wheel speed. Grain growth occurred quickly when sintering at high temperatures with observed grain sizes of several micrometres on the SPSed bulk samples. A single-phase structure with slight phase separation was observed in all SPSed samples. Both electrical and thermal properties were also observed with speed-dependent changes during MS due to the influence of grain growth starting from different morphologies. As a result, the highest ZT value of 1.1 at 823 K was achieved for the optimised wheel rotation speed of 3000 rpm. The results suggest that the optimization of experimental parameters plays a vital role in the strategic enhancement of TE efficiency of melt-spun $Ti_{0.5}Zr_{0.5}NiSn$ alloys and other TE materials.

CRediT author statement

Nguyen Van Du: Conceptualisation, Methodology, Validation, Formal analysis, Data curation, Visualisation, Supervision, Writing - Reviewing and Editing; Nguyen Tu: Data curation, Formal analysis, Writing - Reviewing and Editing; Do Quang Trung: Data curation, Formal analysis, Writing - Reviewing and Editing; Noy Sysavanh: Investigation, Data curation, Writing original draft preparation; Manh Trung Tran: Data curation, Formal analysis, Writing - Reviewing and Editing; Tong Thi Hao Tam: Data curation, Formal analysis, Writing - Reviewing and Editing.

ACKNOWLEDGEMENTS

This research is funded by Vietnam National Foundation for Science and Technology Development (NAFOSTED) under grant number 103.02-2019.356.

COMPETING INTERESTS

The authors declare that there is no conflict of interest regarding the publication of this article.

REFERENCES

[1] K.S. Kim, Y.M. Kim, H. Mun, et al. (2017), "Direct observation of inherent atomic-scale defect disorders responsible for high-performance $Ti_{1-x}Hf_xNiSn_{1-y}Sb_y$ half-Heusler TE alloys", *Advanced Materials*, **29(36)**, pp.1-11, DOI: 10.1002/adma.201702091.

[2] H. Zhao, B. Cao, S. Li, et al. (2017), "Engineering the TE transport in half-Heusler materials through a bottom-up nanostructure synthesis", *Advanced Energy Materials*, **7(18)**, DOI: 10.1002/aenm.201700446.

[3] Z.J. Xu, L.P. Hu, P.J. Ying, et al. (2015), "Enhanced TE and mechanical properties of zone melted p-type $(Bi,Sb)_2Te_3$ TE materials by hot deformation", *Acta Materialia*, **84**, pp.385-392, DOI: 10.1016/j.actamat.2014.10.062.

[4] Y. Pan, U. Aydemir, J.A. Grovogui, et al. (2018), "Melt-centrifuged $(Bi,Sb)_2Te_3$: Engineering microstructure toward high TE efficiency", *Advanced Materials*, **30(34)**, pp.1-7, DOI: 10.1002/adma.201802016.

[5] J. Zhang, L. Zhang, W. Ren, et al. (2021), "Multiple-filling-induced full-spectrum phonon scattering and band convergence leading to high-performance n-type skutterudites", *ACS Applied Materials & Interfaces*, **13(25)**, pp.29809-29819, DOI: 10.1021/acsami.1c06267.

[6] D. Qin, W. Shi, W. Xue, et al. (2020), "Solubility study of Y in n-type $Y_xCe_{0.15}Co_4Sb_{12}$ skutterudites and its effect on TE properties", *Materials Today Physics*, **13**, DOI: 10.1016/j.mtphys.2020.100206.

[7] Y. Liu, H. Xie, C. Fu, et al. (2015), "Demonstration of a phonon-glass electron-crystal strategy in (Hf,Zr)NiSn half-Heusler TE materials by alloying", *Journal of Material Chemistry A*, **45(3)**, pp.22716-22722, DOI: 10.1039/C5TA04418A.

[8] M.N. Guzik, M. Schrade, R. Tofan, et al. (2019), "Long and short-range structures of $Ti_{1-x}Hf_xNi_{1.0/1.1}Sn$ half-Heusler compounds and their electric transport properties", *Cryst. Eng. Comm.*, **21**, pp.3330-3342, DOI: 10.1039/C9CE00046A.

[9] S. Katsuyama, R. Matsuo, M. Ito (2007), "TE properties of half-Heusler alloys $Zr_{1-x}Y_xNiSn_{1-y}Sb_y$", *Journal of Alloys and Compounds*, **428(1-2)**, pp.262-267, DOI: 10.1016/j.jallcom.2006.02.075.

[10] S.W. Kim, Y. Kimura, Y. Mishima (2007), "High temperature TE properties of TiNiSn-based half-Heusler compounds", *Intermetallics*, **15(3)**, pp.349-356, DOI: 10.1016/j.intermet.2006.08.008

[11] L. Chen, Y. Liu, J. He, et al. (2017), "High TE figure of merit by resonant dopant in half-Heusler alloys", *AIP Advances*, **7(6)**, pp.1-6, DOI: 10.1063/1.4986760.

[12] G. Mesaritis, I. Ioannou, A. Delimitis, et al. (2022), "n-type (Zr,Ti)NiSn half Heusler materials via mechanical alloying: Structure, Sb-doping and TE properties", *Journal of Physics and Chemistry of Solids*, **167**, DOI: 10.1016/j.jpcs.2022.110735.

[13] G. Park, H.S. Lee, S. Yi (2022), "Effects of annealing on the microstructure and TE properties of half-Heusler MNiSn (M=Ti, Zr, Hf)", *Journal of Electronic Materials*, **51**, pp.3485-3494.

[14] H.B. Kang, B. Poudel, W. Li, et al. (2020), "Decoupled phononic-electronic transport in multi-phase n-type half-Heusler nanocomposites enabling efficient high temperature power generation", *Materials Today*, **36**, pp.63-72, DOI: 10.1016/j.mattod.2020.01.002.

[15] H. Zhang, Y. Wang, K. Dahal, et al. (2016), "TE properties of n-type half-Heusler compounds $(Hf_{0.25}Zr_{0.75})_{1-x}Nb_xNiSn$", *Acta Materialia*, **113**, pp.41-47, DOI: 10.1016/j.actamat.2016.04.039.

[16] H. Geng, H. Zhang (2014), "Effects of phase separation on the TE properties of (Ti, Zr, Hf)NiSn half-Heusler alloys", *Journal of Applied Physics*, **116(3)**, pp.1-7, DOI: 10.1063/1.4890610.

[17] M. Gürth, G. Rogl, V.V. Romaka, et al. (2016), "TE high ZT half-Heusler alloys $Ti_{1-x-y}Zr_xHf_yNiSn$ ($0\leq x\leq 1$; $0\leq y\leq 1$)", *Acta Materialia*, **104**, pp.210-222, DOI: 10.1016/j.actamat.2015.11.022.

[18] Y. Tang, X. Li, L.H.J. Martin, et al. (2018), "Impact of Ni content on the TE properties of half-Heusler TiNiSn", *Energy & Environmental Science*, **11(2)**, pp.311-320, DOI: 10.1039/C7EE03062B.

[19] N.S. Chauhan, S. Bathula, A. Vishwakarma, et al. (2018), "Vanadium-doping-induced resonant energy levels for the enhancement of TE performance in Hf-free ZrNiSn half-Heusler alloys", *ACS Applied Energy Materials*, **1(2)**, pp.757-764, DOI: 10.1021/acsaem.7b00203.

[20] N.V. Du, W.H. Nam, J.Y. Cho, et al. (2021), "Enhanced TE properties of Hf-free half-Heusler compounds prepared via highly fast process", *Journal of Alloys and Compounds*, **886**, pp.1-10, DOI: 10.1016/j.jallcom.2021.161293.

[21] S.A. Barczak, J. Buckman, R.I. Smith, et al. (2018), "Impact of interstitial Ni on the TE properties of the half-Heusler TiNiSn", *Energy & Environmental Science*, **11(4)**, pp.311-320, DOI: 10.3390/ma11040536.

[22] A. Bahrami, P. Ying, U. Wolff, et al. (2021), "Reduced lattice thermal conductivity for half-Heusler ZrNiSn through cryogenic mechanical alloying", *ACS Applied Materials & Interfaces*, **13(32)**, pp.38561-38568, DOI: 10.1021/acsami.1c05639.

[23] Y. Sun, W. Qiu, L. Zhao, et al. (2020), "Defects engineering driven high power factor of ZrNiSn-based half-Heusler TE materials", *Chemical Physics Letters*, **755**, pp.1-6, DOI: 10.1016/j.cplett.2020.137770.

[24] Y. Xing, R. Liu, J. Liao, et al. (2019), "High-efficiency half-Heusler TE modules enabled by self-propagating synthesis and topologic structure optimization", *Energy & Environmental Science*, **12(11)**, pp.3390-3399, DOI: 10.1039/C9EE02228G.

[25] C. Yu, T.J. Zhu, R.Z. Shi, et al. (2009), "High-performance half-Heusler TE materials $Hf_{1-x}Zr_xNiSn_{1-y}Sb_y$ prepared by levitation melting and spark plasma sintering", *Acta Materialia*, **57(9)**, pp.2757-2764, DOI: 10.1016/j.actamat.2009.02.026.

[26] X. Yang, D. Liu, F. Yang, et al. (2020), "Enhanced TE performance of $Zr_{1-x}Ta_xNiSn$ half-Heusler alloys by diagonal-rule doping", *ACS Applied Materials & Interfaces*, **12(3)**, pp.3773-3783, DOI: 10.1021/acsami.9b21517.

[27] M.M. Al Malki, Q. Qiu, T. Zhu, et al. (2019), "Creep behavior and postcreep TE performance of the n-type half-Heusler alloy $Hf_{0.3}Zr_{0.7}NiSn_{0.98}Sb_{0.02}$", *Materials Today Physics*, **9**, pp.1-7, DOI: 10.1016/j.mtphys.2019.100134.

[28] C.S. Birkel, J.E. Douglas, B.R. Lettiere, et al. (2013), "Improving the TE properties of half-Heusler TiNiSn through inclusion of a second full-Heusler phase: Microwave preparation and spark plasma sintering of $TiNi_{1+x}Sn$", *Physical Chemistry Chemical Physics*, **15(18)**, pp.6990-6997, DOI: 10.1039/c3cp50918d.

[29] C. Yu, T.J. Zhu, K. Xiao, et al. (2009), "Reduced grain size and improved TE properties of melt spun (Hf,Zr)NiSn half-Heusler alloys", *Journal of Electronic materials*, **39**, pp.2008-2012, DOI: 10.1007/s11664-009-1032-8.

[30] L. Chen, C. Zhou, G. Chen, et al. (2015), "Uncovering high TE figure of merit in (Hf,Zr)NiSn half-Heusler alloys", *Applied Physics Letters*, **106(19)**, pp.1-5, DOI: 10.1063/1.4921050.

[31] G. Joshi, T. Dahal, S. Chen, et al. (2013), "Enhancement of TE figure-of-merit at low temperatures by titanium substitution for hafnium in n-type half-Heuslers $Hf_{0.75-x}Ti_xZr_{0.25}NiSn_{0.99}Sb_{0.01}$", *Nano Energy*, **2(1)**, pp.82-87, DOI: 10.1016/j.nanoen.2012.07.020.

[32] S. Chen, K.C. Lukas, W. Liu, et al. (2013), "Effect of Hf concentration on TE properties of nanostructured N - type half-Heusler materials $Hf_xZr_{1-x}NiSn_{0.99}Sb_{0.01}$", *Advanced Energy Materials*, **3(9)**, pp.1210-1214, DOI: 10.1002/aenm.201300336.

[33] S. Populoh, M.H. Aguirre, O.C. Brunko, et al. (2012), "High figure of merit in (Ti,Zr,Hf)NiSn half-Heusler alloys", *Scripta Materialia*, **66(12)**, pp.1073-1076, DOI: 10.1016/j.scriptamat.2012.03.002.

[34] G. Rogl, P. Sauerschnig, Z. Rykavets, et al. (2017), "(V,Nb)-doped half-Heusler alloys based on {Ti,Zr,Hf}NiSn with high ZT", *Acta Materialia*, **131**, pp.336-348, DOI: 10.1016/j.actamat.2017.03.071.

[35] N.S. Chauhan, P.R. Raghuvanshi, K. Tyagiet, et al. (2020), "Defect engineering for enhancement of TE performance of (Zr, Hf)NiSn-based n-type half-Heusler alloys", *Journal of Physical Chemistry C*, **124(16)**, pp.8584-8593, DOI: 10.1021/acs.jpcc.0c00681.

[36] Q. Zhang, P. Xie, C. Liu, et al. (2022), "Enhanced TE performance of hafnium free n-type ZrNiSn half-Heusler alloys by isoelectronic Si substitution", *Materials Today Physics*, **24**, pp.1-7, DOI: 10.1016/j.mtphys.2022.100648.

[37] X. Zhang, S. Li, B. Zou, et al. (2022), "Significant enhancement in TE properties of half-Heusler compound TiNiSn by grain boundary engineering", *Journal of Alloys and Compounds*, **901**, pp.1-7, DOI: 10.1016/j.jallcom.2022.163686.

[38] H. Xie, H. Wang, C. Fu, et al. (2014), "The intrinsic disorder related alloy scattering in ZrNiSn half-Heusler TE materials", *Scientific Reports*, **4(11)**, DOI: 10.1038/srep06888.

[39] R.A. Downie, S.R. Popuri, H. Nin, et al. (2014), "Effect of spark plasma sintering on the structure and properties of $Ti_{1-x}Zr_xNiSn$ half-Heusler alloys", *Materials*, **7(10)**, pp.7093-7104, DOI: 10.3390/ma7107093.